Spectral properties of superconducting microwave photonic crystals modeling Dirac billiards

B. Dietz,* T. Klaus, M. Miski-Oglu, and A. Richter
Institut für Kernphysik, Technische Universität Darmstadt, D-64289 Darmstadt, Germany
(Received 17 October 2014; revised manuscript received 9 December 2014; published 12 January 2015)

We determined experimentally the eigenvalues of two rectangular quantum billiards that contain circular scatterers forming a triangular grid, so-called Dirac billiards. For this we performed measurements of unprecedented accuracy using superconducting macroscopic-size microwave billiards that enclose a photonic crystal. The objective was the investigation of the peculiar features of the density of the eigenvalues (DOE), which resemble that of a graphene flake, and of their fluctuation properties. We identified in the measured resonance spectra Dirac points and in their adjacent bands the van Hove singularities (VHSs), that show up as sharp peaks in the DOE. The analysis of the experimental resonance frequencies and of the band structure, which was computed with a tight-binding model, revealed that the VHSs divide the associated band into regions where the system is governed by the nonrelativistic Schrödinger equation of the quantum billiard and the Dirac equation of the graphene billiard of corresponding shape, respectively. Furthermore, we demonstrate that Dirac billiards are most suitable for the modeling of idealized graphene. Indeed, the DOEs of both systems are well described by a finite tight-binding model which includes first-, second-, and third-nearest-neighbor couplings.

DOI: 10.1103/PhysRevB.91.035411 PACS number(s): 42.70.Qs, 73.22.Pr, 42.25.Fx

I. INTRODUCTION

The pioneering fabrication of graphene [1], a crystalline monolayer of carbon atoms forming a honeycomb lattice, triggered by reason of its extraordinary properties an immense amount of experimental and theoretical investigations. The most intriguing one is a linear dispersion relation near the Fermi energy, i.e., in the vicinity of the so-called Dirac points [2] (DPs) that are located at the corners of the hexagonal Brillouin zone (BZ). There the conduction and valence bands touch each other conically so the electronic excitations behave as massless Dirac fermions. Consequently, near the DPs the electronic properties of graphene are described by a Dirac equation and, even though the Fermi velocity of the electrons is by a factor of 300 smaller than that of light, it features relativistic phenomena [2–6].

In recent years, graphene quantum dots, so-called graphene billiards, have been the focus of experimental activities [7–11]. The experiments that are the subject of this paper were motivated by the nonconforming results on their spectral properties. They were investigated experimentally in Ref. [8] and numerically in Refs. [12–14]. While the former revealed that they coincide with those of neutrino billiards of corresponding shape [15,16], that is, with those of random matrices from the Gaussian unitary ensemble (GUE), the latter found agreement with those from the Gaussian orthogonal one (GOE) [17–19]. Indeed, these ensembles are applicable to generic chaotic systems with and without violated time-reversal invariance, respectively. The discrepancies were attributed to the differing conditions on the wave functions along the boundaries (see Ref. [20]). In a subsequent publication [21], graphene billiards were studied analytically where the focus was the influence of different edge geometries on the properties of the density of the electronic excitations of graphene billiards.

The focus of this paper are the properties of the resonance density and of the spectra of two macroscopic-size rectangular microwave Dirac billiards providing an experimental realization of idealized graphene flakes or quantum dots as outlined in Ref. [22]. Here, we exploited the fact that the peculiar band structure of graphene stems from the symmetries of its honeycomb structure which is formed from two interpenetrating triangular lattices with threefold symmetry. Indeed, the manufacturing of artificial graphene using two-dimensional electron gases subject to a honeycomb potential lattice [23,24], molecular assemblies arranged on a copper surface [25], ultracold atoms in optical lattices [26,27] and photonic crystals [28–36] is a rapidly emerging field.

The microwave Dirac billiards, shown in Fig. 1 with the top plates removed, were constructed from photonic crystals, composed of metallic cylinders and arranged on a triangular lattice, that were squeezed into a rectangular microwave cavity [22]. Below a certain frequency, which is inversely proportional to the height of the cavity, the Helmholtz equation describing such systems is two dimensional and mathematically equivalent to the Schrödinger equation of the corresponding quantum billiard [37–39]. Thus, their eigenfrequencies yield the eigenvalues of a rectangular billiard with the same side lengths, which contains circular scatterers at the positions of the cylinders, i.e., of a rectangular Dirac billiard. Due to the presence of the cylinders, the frequencies of wave propagation as function of the two quasimomentum components exhibit a band structure which is similar to that of graphene. Accordingly, the resonance spectra of microwave Dirac billiards contain DPs, where they are expected to be governed by the relativistic Dirac equation. Note that, like the carbon atoms in graphene, the voids between the cylinders of the microwave Dirac billiards, marked by red (gray) and blue (dark gray) dots in Fig. 2, exhibit a hexagonal configuration.

In a previous experiment [31], we used unbounded photonic crystals consisting of cylinders forming a triangular grid and squeezed between two metal plates to perform transmission measurements with plane waves traversing the photonic crystal. These measurements revealed the extremal transmission behavior also observed in graphene in the vicinity of the DP. The aim of the present experiments was the determination of the eigenvalues of Dirac billiards in high-resolution

*dietz@ikp.tu-darmstadt.de

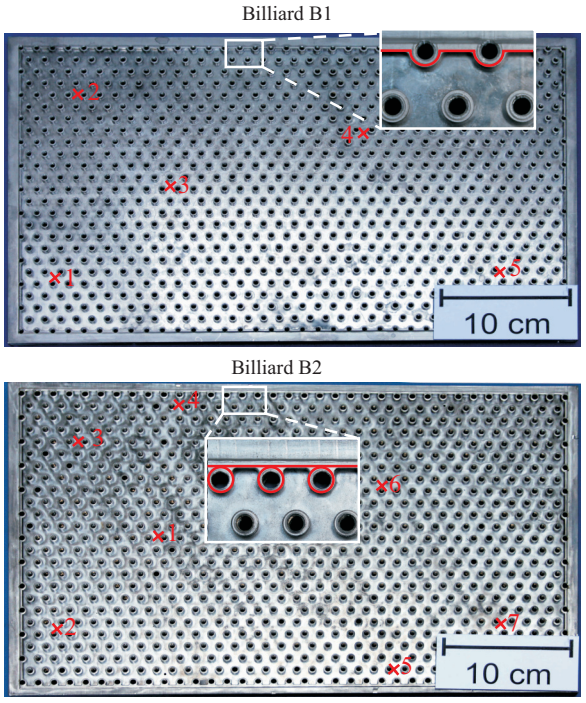

FIG. 1. (Color online) Photographs of the basin plates of the microwave Dirac billiards B1 (upper panel) and B2 (lower panel), each containing 888 metal cylinders. They were constructed from brass and coated with lead to achieve superconductivity at liquid helium temperature. The red (gray) crosses mark the positions of the antennas. The insets show a magnification of the lattice structure along the long sides.

measurements with superconducting microwave billiards [40] and the investigation of their spectral properties in the two frequency bands that frame each DP. These were compared with those of relativistic graphene billiards and nonrelativistic quantum billiards of corresponding shape, respectively. As outlined in Ref. [21], depending on the boundary structure of a graphene billiard it may exhibit edge states [35,41–43]. We performed experiments with two different microwave billiards, one with and one without edge states.

The paper is organized as follows. In Sec. II, the experimental setup is introduced. The measured resonance spectra and

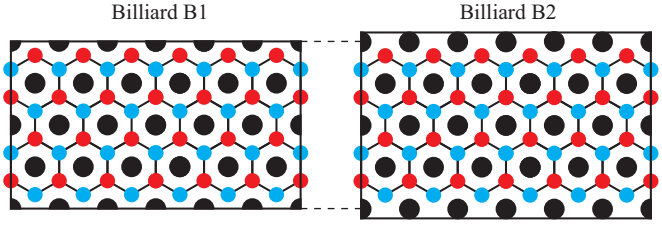

FIG. 2. (Color online) Schematic view of the triangular lattice structure of billiards B1 (left-hand side) and B2 (right-hand side). The red (gray) and blue (dark gray) dots mark the voids between the cylinders. They correspond to the atoms in graphene, that generate the two independent triangular lattices. In both billiards, the resulting hexagonal lattice is terminated by armchair and zigzag edges along the short and the long sides, respectively. In billiard B1 it is translationally invariant with respect to all sides, in B2 only along the short ones.

their salient properties are presented in Sec. II B. In Sec. III, the resonance density extracted from the resonance spectra is compared to results obtained with tight-binding models (TBM) for unbounded and for bordered graphene sheets. The focus of Secs. IV and V are the spectral properties in the bands that frame each of the two DPs found in the spectra of both billiards.

II. EXPERIMENT

A. Experimental setup

The experiments were performed for two superconducting Dirac billiards [22,31] called B1 and B2 in the sequel. They consisted of a brass lid and a rectangular basin with side lengths 420.0×249.4 mm^2 and 420.0×255.4 mm^2 for B1 and B2, respectively. For the construction of the basin, 888 metallic cylinders were milled out of a brass plate. The lattice constant was $a_L = 12$ mm and the radius of the cylinders was $R = a_L/4$. Figure 1 displays the bottom plates of B1 and B2. The billiards differ in the structure of the lattice edges along the long sides. In B1, the lattice ends there with half cylinders and in B2 with full ones. This is clearer visible in Fig. 2 where the billiards are depicted schematically. The metallic cylinders are arranged on a triangular lattice, so the voids between the cylinders form a hexagonal one as indicated by the colored dots. In fact, three neighboring cylinders constitute a triangular cell that hosts a quasibound state localized at its center and thus can be considered as an open resonator. Accordingly, the lattice can be regarded as being composed of coupled resonators centered at the voids, acting as the carbon atoms in graphene and forming the two independent triangular sublattices marked by red (gray) and blue (light gray) dots in Fig. 2. In both billiards, this void structure is terminated with armchair and zigzag edges along the short and the long sides of the rectangular billiard, respectively. Due to the geometry of the lattice formed by the cylinders at the edges, B1 can be expanded over the whole plane by reflections at its sidewalls, i.e., it can be considered as an infinitely extended lattice with periodic boundary conditions whereas this is not the case for B2. Accordingly, we expect the occurrence of edge states in B2, whereas they should be absent in B1 [21].

In order to attain superconductivity at liquid helium temperature, the lids and the basins of the microwave billiards were lead coated. A proper electrical contact was achieved by screwing the former tightly to each cylinder of the latter. The height of the Dirac billiards was $h = 3$ mm. Accordingly, for frequencies below 50 GHz only the lowest transverse magnetic mode with the electric field vector perpendicular to the top and bottom plates was excited. Thus, in that frequency range, the microwaves inside the resonator were governed by the scalar Helmholtz equation which is mathematically identical to the Schrödinger equation of the corresponding two-dimensional rectangular quantum billiard [37–39] with Dirichlet boundary conditions at the walls of the cavity and of the scatterers.

B. Resonance spectra

For the measurement of the transmission spectra, microwave power was emitted into the resonator via one wire antenna and a vectorial network analyzer (VNA) determined

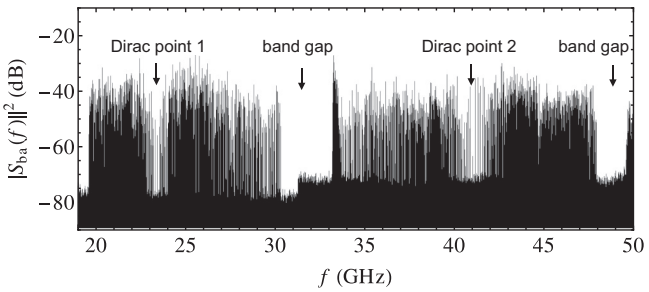

FIG. 3. Transmission spectrum of the Dirac billiard B1. The stop band terminates at 19.61 GHz. The spectrum exhibits two band gaps and two DPs that are framed by regions of low resonance density. The part below the first band gap has been shown in Ref. [22]. The lower band gap is terminated by a narrow region of exceptionally high density.

the relative phase and amplitude of the output and input signals. Altogether, five antennas were attached to the lid of B1 and seven to that of B2. Their positions are marked by red (gray) crosses in the upper and the lower panels of Fig. 1 for B1 and B2, respectively. They reached a few millimeters into the resonator through holes in the lid. The positions of the resonances in the transmission spectra yielded the eigenfrequencies of the Dirac billiards. The measurements were performed with all possible antenna combinations in order to make sure that no resonances were missing. This could occur if one of the antennas is positioned at a nodal line of the electric field intensity inside the resonator so that the resonance cannot be excited [44]. Due to the high-quality factors $Q > 5 \times 10^5$ of the resonances, we could resolve all of them and thus determined ≈ 4900 eigenfrequencies for B1 and B2 below 50 GHz.

Figure 3 shows a transmission spectrum measured with B1. The first resonances were detected above 19.61 GHz where the stop band terminates. The spectrum exhibits two further band gaps, where the transmission is reduced by four orders of magnitude and no propagation is possible. Furthermore, two regions of low-resonance density are visible. They are located around the Dirac frequencies of the two DPs.

In Fig. 4, we compare the density of the eigenfrequencies (DOE) $\rho(f) = \sum_n \delta(f - f_n)$ for the eigenfrequencies f_n of B1 extracted from the transmission spectrum shown in Fig. 3, with the calculated band-structure function $f(\vec{q})$. The left part displays the experimentally determined DOE. Shown is actually the smoothed DOE, which is obtained by replacing the δ functions by Lorentzians of finite width Γ_L,

$$\rho(f) \simeq \sum_n \frac{1}{\pi} \frac{\Gamma_L}{(f - f_n)^2 + \Gamma_L^2}, \qquad (1)$$

where we chose $\Gamma_L = 40$ MHz. The right part of Fig. 4 shows the calculated band structure along the path ΓMKΓ inside the first Brillouin zone (BZ) depicted in the inset. Here, K denotes the distance of the DPs, that are located at the corners of the BZ, from its center Γ where the corresponding band terminates, M that of the saddle points [2] (see inset of Fig. 4). The positions of the experimental band gaps are in good agreement with those in the calculated band structure. Furthermore, the

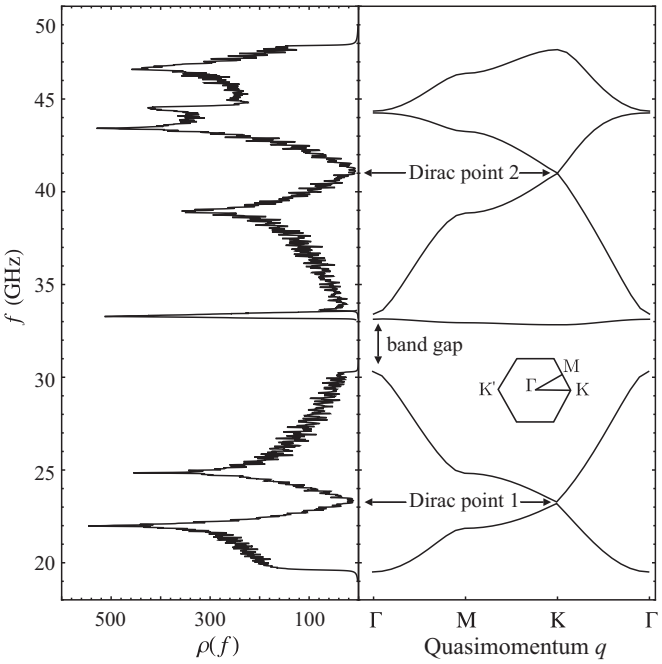

FIG. 4. Comparison of the DOE determined from the measured spectra of B1 (left panel) with the computed band structure of an infinitely extended photonic crystal with the same lattice constant (right panel). The locations of the DPs and the band gaps coincide. Furthermore, the frequencies of the VHSs and the other peaks of $\rho(f)$ agree well with those of the saddle points and the regions of a flat band structure, respectively.

DOE exhibits two broad minima at the frequencies of the DPs indicated in the transmission spectrum shown in Fig. 3. Their locations coincide with those of the Dirac or K points in the calculated band structure where two bands touch each other [45]. They are bordered by sharp peaks, the van Hove singularities [46] (VHSs), that correspond to saddle points in the latter. Generally, the maxima of $\rho(f)$ occur at frequencies where the band barely changes with the quasimomentum, i.e., regions of low group velocity $|\vec{\nabla} f(\vec{q})| \simeq 0$ with $\vec{q}$ being the quasimomentum vector. Particularly, the narrow region of exceptionally high-resonance density at the upper edge of the first band gap in Figs. 3 and 4 is associated with a band that is entirely flat.

The only difference between the transmission spectra of B1 and B2 lies in the accumulation of resonances observed in the latter above the first DP. It is clearly visible in Fig. 5 where a zoom into that region is displayed for B1 (upper panel) and B2 (lower panel). In a previous experiment [31] with a rectangular microwave Dirac billiard containing only 273 metallic cylinders, we demonstrated that, similar to the edge states occurring in graphene flakes, the associated wave-function intensities are nonvanishing only along the zigzag edges. Here, we used the analogy between the wave functions of a quantum billiard and the electric field strength distributions in the corresponding microwave billiard to determine them experimentally. For most of the eigenfrequencies within the range of the accumulation observed in Fig. 5, the field intensity was nonvanishing only

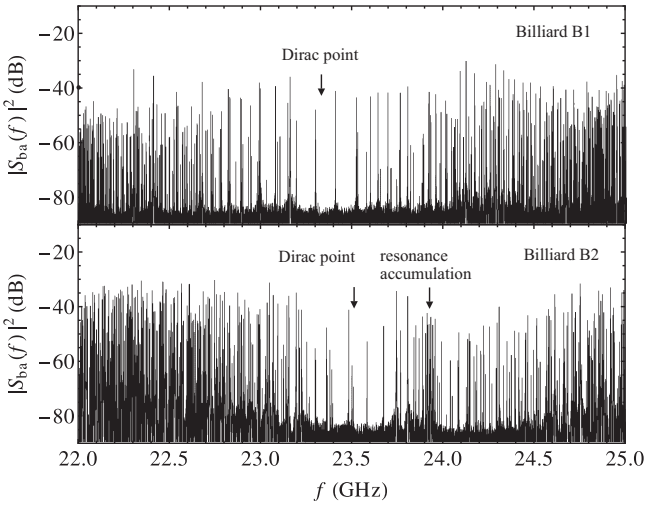

FIG. 5. Comparison of the zooms into the transmission spectra around the first DP of billards B1 (upper panel) and B2 (lower panel). An accumulation of the resonances is clearly observable above the DP in the lower panel. These are associated with edge states located along the long sides of the Dirac billiard B2 (see main text).

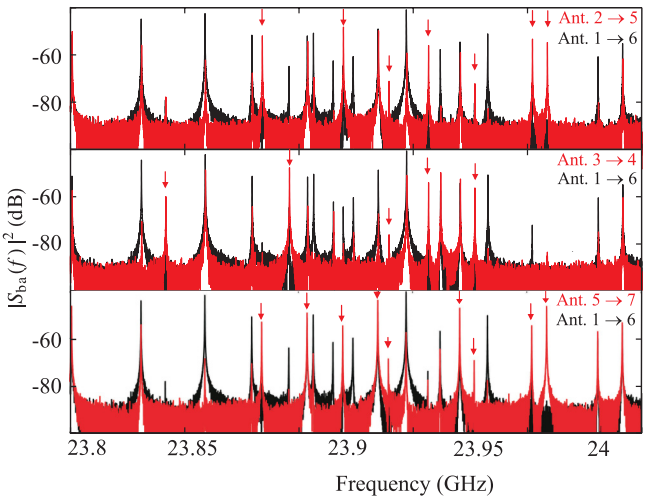

FIG. 6. (Color online) Comparison of transmission spectra of B2 in the region of the resonance accumulation. They were measured between antennas 1 and 6 located in the interior of the billiard (black) and with antennas 2, 3, 4, 5, and 7 positioned close to the edges [red (gray)]. The antenna positions are marked in the lower panel of Fig. 1. Resonances that were only excited by the border antennas [marked by red (gray) arrows] are associated with edge states.

along the long sides of the billiard, i.e., the zigzag edges, whereas it was distributed over the billiard plane otherwise.

Because of the large number of closely lying metallic cylinders, a direct measurement of the wave functions was not possible with the billiards considered in this paper. Therefore, in order to test whether the states from the region of resonance accumulation correspond to edge states with intensities localized at the zigzag edges of B2, we used the fact that the resonance amplitudes in a spectrum are proportional to the field strengths at the positions of the antennas [44]. Accordingly, we measured transmission spectra with antennas positioned close to the edges of B2 and in its interior. The different antenna positions of B2 are marked by red (gray) crosses in the lower panel of Fig. 1. In Fig. 6, we compare the spectrum taken with the interior antennas 1 and 6 (black) with those obtained with antennas positioned close to the short (armchair) edges, i.e., antennas 2, 3, and 7 and near the long (zigzag) edges, marked as 4 and 5. Peaks pointed at with red arrows correspond to resonances that do not show up in the spectrum obtained with antennas positioned in the interior of the resonator. They thus correspond to edge states.

III. TIGHT-BINDING MODEL DESCRIPTION

In this section and in Sec. IV, we restrict to the two bands of billiards B1 and B2 that are joined at the lower DP. Figure 7 shows the DOE $\rho(f)$ inferred from the measured spectra using Eq. (1). Due to the presence of the photonic crystal inside the microwave billiard, the DOE clearly deviates from that of an empty one [40,47], which according to Weyl's law [48] should increase linearly with f. The region around its minimum at the Dirac frequency is bordered by two sharp peaks at f_{VH}^{-} and f_{VH}^{+}. As already noted, these are the VHSs [46]. There, $\rho(f)$ diverges logarithmically for two-dimensional periodic structures of infinite extent. In the Dirac billiards used in the experiments, however, the peaks have a finite height $\rho^{\max}$. Its

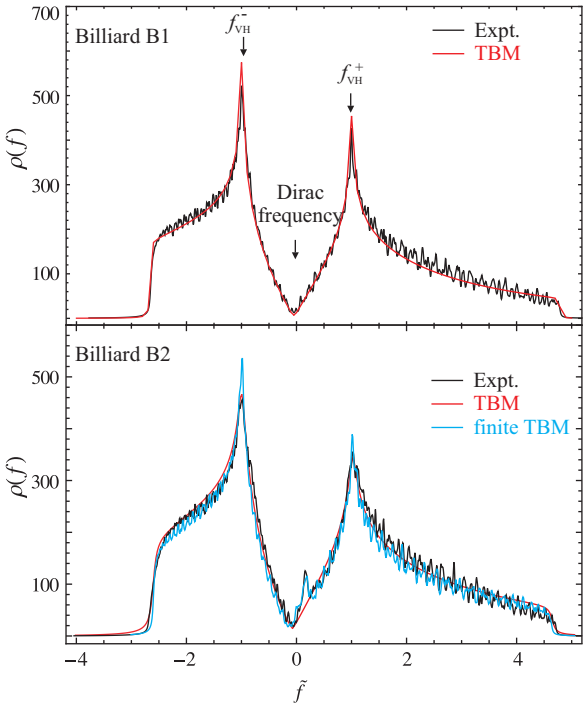

FIG. 7. (Color online) Comparison of the DOE obtained from the spectra (black) of B1 (upper panel) and B2 (lower panel) with that resulting from the TBM for an infinitely extended photonic crystal with the same lattice constant [red (gray)]. Here, the eigenfrequencies were shifted and rescaled such that the Dirac point is at $\tilde{f} = 0$ and the distance of the VHSs equals 2 [22]. In the lower panel, the small peak to the right of the DP is due to edge states. It is well described by a finite TBM for a photonic crystal of the same size as the one used in the experiments with special boundary conditions along the zigzag edges [blue (light gray)].

TABLE I. Frequencies in GHz of the lower (f_{lBE}) and the upper (f_{uBE}) band edges, the DP (f_D), and the VHSs ($f_{\mathrm{VH}}^{\pm}$) of billiards B1 and B2.

	f_{lBE}	f_{VH}^{-}	f_D	f_{VH}^{+}	f_{uBE}
B1	19.64	21.98	23.36	24.87	30.15
B2	19.98	22.23	23.53	25.15	30.20

dependence on the area of the associated photonic crystal has been investigated in Ref. [22]. The frequencies at the DPs f_D, the VHSs $f_{\mathrm{VH}}^{\pm}$, and the lower and the upper band edges f_{lBE} and f_{uBE}, respectively, are given in Table I. The oscillations of the experimental $\rho(f)$ around its mean value differ in the frequency ranges in-between the two VHSs and below and above them. The focus of this paper is the investigation of the spectral properties that in fact are strongly linked to these fluctuations. We show in Sec. IV A that in the frequency ranges below f_{VH}^{-} and above f_{VH}^{+}, they coincide with those of an empty quantum billiard of corresponding shape, which is described by the Schrödinger equation. This defines the *nonrelativistic* region. In Sec. IV B, we demonstrate that in the region around the Dirac frequency f_{D}, on the other hand, they are similar to those of relativistic graphene billiards [21]. Since these are governed by the Dirac equation [49] we call this part of the band structure the *relativistic* region.

The red curves in Fig. 7 show the result of a tight-binding model (TBM) computation. The first TBM description of graphene was provided by Wallace [50]. He took into account only nearest- and second-nearest-neighbor interactions for the graphene p_z orbitals, but neglected the overlap between the wave functions centered at the different atoms. We used the TBM approach for an infinitely extended hexagonal lattice structure such as graphene described in Ref. [51]. In that model, the band-structure function, i.e., the dependence of the frequencies $f(\vec{q})$ on the quasimomentum vector $\vec{q}$, is obtained by solving the generalized eigenvalue problem

$$\mathcal{H}_{\mathrm{TBM}}|\Psi_{\vec{q}}(\vec{r})\rangle = f(\vec{q})\mathcal{S}_{\mathrm{WO}}|\Psi_{\vec{q}}(\vec{r})\rangle \tag{2}$$

with the TBM Hamiltonian

$$\mathcal{H}_{\mathrm{TBM}} = \begin{pmatrix} \gamma_0 + \gamma_2 h_2(\vec{q}) & \gamma_1 h_1(\vec{q}) + \gamma_3 h_3(\vec{q}) \\ \gamma_1 h_1(\vec{q}) + \gamma_3 h_3(\vec{q}) & h_0 + \gamma_2 h_2(\vec{q}) \end{pmatrix} \tag{3}$$

and the wave-function overlap matrix

$$\mathcal{S}_{\mathrm{WO}} = \begin{pmatrix} 1 + s_2 h_2(\vec{q}) & s_1 h_1(\vec{q}) + s_3 h_3(\vec{q}) \\ s_1 h_1(\vec{q}) + s_3 h_3(\vec{q}) & 1 + s_2 h_2(\vec{q}) \end{pmatrix}. \tag{4}$$

In distinction to the TBM description [50], this model incorporates the nearest-neighbor coupling γ_1 as well as the second- and third-nearest-neighbor couplings γ_2 and γ_3 and in addition the corresponding overlaps s_1, s_2, and s_3. The functions $h_n(\vec{q})$, $n = 1,2,3$, associated with the different couplings were obtained as outlined in Ref. [51].

The parameters were determined from a fit of the DOE deduced from the band-structure function $f(\vec{q})$ to the experimental one. In order to achieve a good agreement of the DOEs deduced from the TBM and the experimental eigenfrequencies, respectively, we actually had to take into account nearest-neighbor, second- and third-nearest-neighbor couplings between the quasibound states, i.e., the electric field mode components localized at the voids between the metallic cylinders and also the corresponding overlaps. This indicates that the quasibound states slightly extend into the regions of neighboring voids. Still, their coupling is so weak that the TBM is applicable. Indeed, the agreement between the calculated DOE [red (gray)] and the experimental one (black) in Fig. 7 is very good for B1 (upper panel). This TBM, however, does not describe the small peak observed to the right of the Dirac frequency for B2 (lower panel). The peak, actually, is due to the edge states, i.e., it is a finite-size effect, which obviously is not accounted for by the TBM for infinitely extended hexagonal lattices.

The blue curve in the lower panel was obtained from a finite TBM for a bounded hexagonal lattice that had the same size as the one formed by the voids of the microwave photonic crystal in B2. The determination of the associated DOE implies the diagonalization of a (1656×1656)-dimensional TBM matrix. We again included up to third-nearest-neighbor couplings and the corresponding overlaps and used the same parameters γ_0, γ_n, $n = 1,2,3$, and s_n, $n = 1,2,3$, for the fitting procedure as obtained with the TBM equation (2). Furthermore, we accounted for the effect of the lattice structure along the zigzag edges by imposing there special boundary conditions. For B1, we realized periodic boundary conditions by introducing a coupling between opposite atoms of the zizag edges [52]. The resulting DOE is indistinguishable from the one shown in the upper panel of Fig. 7 so we do not show it. In billiard B2 we took the edge effects into account by introducing a potential along the zigzag edges [53]. For this we replaced the parameter γ_0, which describes the onsite potential, by a variable parameter γ_{edge} and determined it from a fit of the resulting DOE to the experimental one. This yielded $\gamma_{\mathrm{edge}} = 0.272$. The good agreement between the DOE obtained from the finite TBM and the experimental one corroborates the assumption that the resonance accumulation observed in the transmission spectrum and the DOE of B2 indeed is an effect of the zigzag edges. We should note that in the simplest TBM for hexagonal lattices possessing zigzag-type edge segments, which includes only nearest-neighbor couplings and no wave-function overlaps, the DOE exhibits a peak at the Dirac frequency. As stated in Ref. [43], at least nonvanishing second-nearest-neighbor couplings are needed to explain the shift of the energy of the edge states with respect to the Dirac frequency observed in graphene sheets. So, the fact that the peak shows up above the Dirac frequency in the lower panel of Fig. 7 already indicates that the simplest TBM does not describe the experimental DOE. The results for the coupling and the overlap parameters are given in Table II.

TABLE II. Coupling parameters in GHz and overlap parameters resulting from a fit of the DOE deduced from the TBM equation (2) to the experimental one.

	γ_0	γ_1	γ_2	γ_3	s_1	s_2	s_3
B1	0.011	1.009	0.022	−0.013	−0.060	−0.023	−0.009
B2	0.007	1.008	0.038	−0.011	−0.062	−0.020	0.002

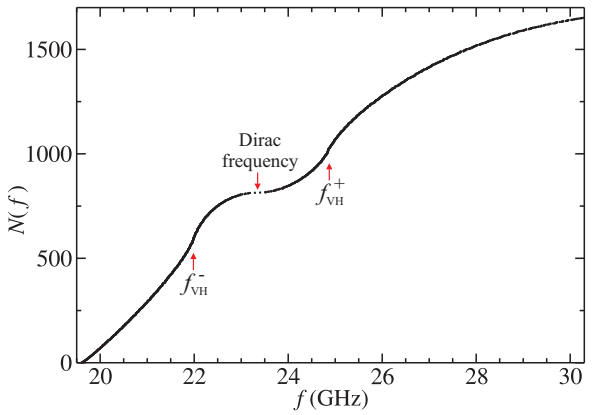

FIG. 8. (Color online) The integrated DOE $N(f)$ obtained for the first two bands of the resonance spectrum shown in Fig. 3 that are joined at the first DP. It exhibits a plateau around the Dirac frequency $f_D = 23.36$ GHz and barely visible kinks at the frequencies $f_{VH}^{-} = 21.98$ GHz and $f_{VH}^{+} = 24.87$ GHz of the VHSs. Adopted from Ref. [22].

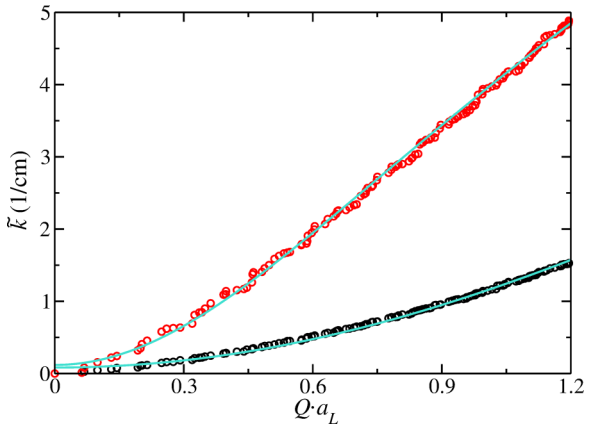

FIG. 9. (Color online) The wave numbers of B1 plotted in the lower Schrödinger region $\tilde{k} = \tilde{k}_l$ as black circles and in the upper one $\tilde{k} = \tilde{k}_u$ as red (gray) ones versus the eigenvalues $Q = q_S$ of the rectangular quantum billiard with the same side lengths as the Dirac billiard. The turquoise (light gray) full lines show the band-structure function $\tilde{k} = 2\pi f(\delta\vec{q})/c$, which was computed by inserting the TBM parameters listed in Table II into the analytical expression given in Ref. [51] versus the distance $Q = |\delta\vec{q}|$ of the quasimomentum vector $\vec{q}$ from the Γ point.

IV. SPECTRAL PROPERTIES AND LENGTH SPECTRA OF B1

In this section, we analyze the integrated DOE, the length spectra, the nearest-neighbor spacing distribution, and the Δ_3 statistics as measures for the fluctuation properties of the eigenfrequencies of the Dirac billiard B1. Since the results are similar for both Dirac billiards, we do not present them for B2. Figure 8 shows the integrated DOE $N(f)$ determined for the frequency range under consideration, i.e., for the two bands framing the lower DP in the measured resonance spectra, as function of the excitation frequency f. It exhibits a plateau in the region around the Dirac frequency f_D, the Dirac region, which stems from the low DOE in that frequency range (see Fig. 3). Above and below f_D it has the shape of half a parabola opening upwards and downwards, respectively. Furthermore, it has barely visible kinks at the frequencies $f_{VH}^{\pm}$ of the VHSs. In the regions below f_{VH}^{-} and above f_{VH}^{+}, the Schrödinger region, the frequency dependence is different from that in-between. We investigated the transition from the Dirac to the Schrödinger region that takes place at the VHSs in a previous paper [22]. Sections IV A and IV B are devoted to the features of the spectra in these regions. To be more explicit, we compare the integrated DOE, the length spectra and fluctuation properties of the eigenfrequencies of the Dirac billiard in the Schrödinger region with those of the eigenvalues of an empty quantum billiard (QB) governed by the Schrödinger equation, in the Dirac region with those of a graphene billiard (GB) which is described by the Dirac equation, both having the same shape as the former one.

A. Schrödinger region

In this section, we consider the spectral properties of the lower and the upper Schrödinger regions, i.e., of the smallest and the largest 250 wave numbers $\tilde{k}_{l,n} = k_n - k_{lBE}$, $n = 1, \ldots, 250$, and $\tilde{k}_{u,\tilde{n}} = |k_n - k_{uBE}|$, $n = 1402, \ldots, 1651$, $\tilde{n} = 1652 - n$, respectively. Here, $k_n = 2\pi f_n/c$ is deduced from the experimentally determined eigenfrequencies f_n and, similarly, k_{lBE} and k_{uBE} are obtained from the eigenfrequencies f_{lBE} and f_{uBE} at the lower and the upper band edges, respectively. Their values are given in Table I. We also computed the wave functions associated with these wave numbers using the finite TBM introduced in Sec. III and found that they coincide with those of a rectangular quantum billiard with the same side lengths as B1. The latter is governed by the Schrödinger equation $(\frac{\partial^2}{\partial x^2} + \frac{\partial^2}{\partial y^2} + q_{QB}^2)\psi_{QB}(x,y) = 0$ with the Dirichlet condition along its boundary $\partial\Omega$, i.e., $\psi_{QB}(x,y)|_{\partial\Omega} = 0$, for $(x,y) \in \Omega$ where Ω denotes its interior. Accordingly, we plotted in Fig. 9 the wave numbers of B1 in the lower Schrödinger region $\tilde{k} = \tilde{k}_l$ as black circles and in the upper one $\tilde{k} = \tilde{k}_u$ as red (gray) ones against the eigenvalues $Q = q_S = q_{QB} - q_{QB0}$ of the rectangular quantum billiard, with q_{QB0} denoting the smallest one. The latter were shifted such that the smallest eigenvalue equaled zero as is the case for the spectra of $\tilde{k}_l, \tilde{k}_u$. We compared both curves with the band-structure function $f(\vec{q})$ defined in Eq. (2). To compute it, we inserted the tight-binding parameters listed in Table II into the analytical expression provided in Ref. [51]. In Fig. 9, the turquoise (light gray) full lines show $f(\delta\vec{q})$ in a region close to the Γ point, i.e., to the lower and upper band edges, versus the distance of the quasimomentum vector $\vec{q}$ from it, $Q = |\delta\vec{q}|$. The good agreement, first, corroborates the applicability of the TBM to the experimental data and, second, proves that the quasimomenta $|\delta\vec{q}|$ indeed may be identified with the eigenvalues of the rectangular quantum billiard. Both the experimental and the TBM curves are well approximated by a quadratic polynomial in the lower Schrödinger regime, and also in the upper one after skipping the $\approx$10 lowest eigenfrequencies.

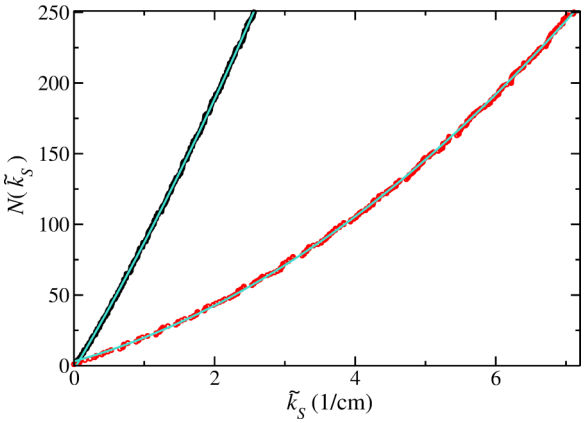

FIG. 10. (Color online) Integrated DOEs of B1 in the lower ($\tilde{k}_S = \tilde{k}_l$) and the upper ($\tilde{k}_S = \tilde{k}_u$) Schrödinger regions are depicted as black circles and as red (gray) ones, respectively. The quadratic polynomials that describe the data best are plotted as turquoise (light gray) full lines.

1. Integrated DOE and length spectra

This clear correspondence between the wave numbers of B1 and the eigenvalues of the rectangular quantum billiard is corroborated by the similarity of the fluctuating parts of the associated integrated DOEs. Figure 10 displays the integrated DOE obtained for the wave numbers $\tilde{k}_S = \tilde{k}_l$ (black dots) and $\tilde{k}_S = \tilde{k}_u$ [red (gray) dots] of the lower and the upper Schrödinger regions, respectively. Both curves are best fit by a quadratic polynomial plotted as turquoise (light gray) full line yielding the smooth part of the integrated DOE N_{smooth}.

The fluctuating part $N_{\text{fluc}}(\tilde{k}_S) = N(\tilde{k}_S) - N_{\text{smooth}}(\tilde{k}_S)$ is plotted in Figs. 11 and 12 for the wave numbers in the lower ($\tilde{k}_S = \tilde{k}_l$) and the upper ($\tilde{k}_S = \tilde{k}_u$) Schrödinger regions, respectively, as black circles, and as red ones for the corresponding quantum billiard, versus the eigenvalues of the latter. For better visibility, the data points are joined by dashed lines. Similarly, the agreement of the length spectra determined from

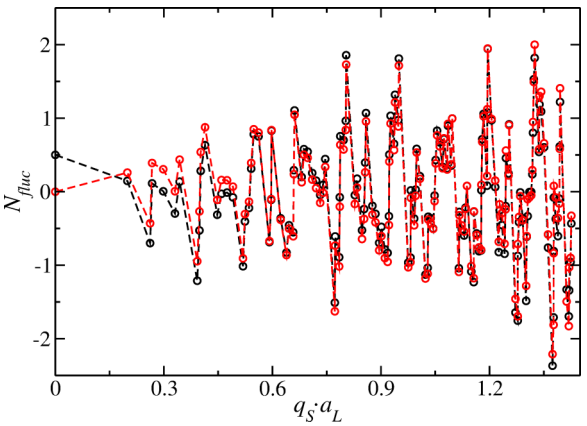

FIG. 11. (Color online) Comparison of the fluctuating parts of the integrated DOE of B1 in the lower Schrödinger region (black circles) with that of the corresponding quantum billiard [red (gray) circles]. For better visibility, the circles are connected by dashed lines of corresponding color.

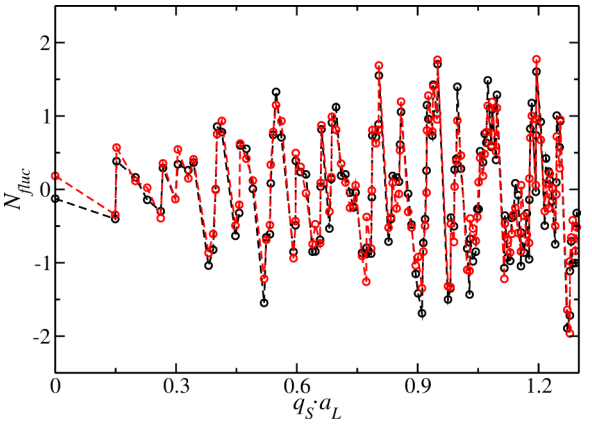

FIG. 12. (Color online) Same as Fig. 11 but for the upper Schrödinger region.

the Fourier transforms of these curves is very good (see Figs. 13 and 14). They, actually, exhibit peaks at the lengths of the periodic orbits in the rectangular quantum billiard [54,55].

2. Spectral properties of the wave numbers

We also analyzed the spectral properties of the wave numbers $\tilde{k}_l, \tilde{k}_u$. For this, we first unfolded the latter by replacing the wave numbers $\tilde{k}_l, \tilde{k}_u$ with the values attained by the polynomial $N_{\text{smooth}}(\tilde{k}_S)$, $\tilde{k}_S = \tilde{k}_l, \tilde{k}_u$ best fitting the corresponding integrated DOE (see Fig. 10). Figure 15 shows as black full line the experimental result for the distribution P(s) of the spacings s between adjacent eigenvalues for the upper Schrödinger region, the black dashed line that for the eigenvalues of the rectangular quantum billiard, and in red (gray) the Poissonian distribution, which applies to generic integrable systems [17,56,57]. Figure 16 shows the Dyson-Mehta statistic [18] Δ_3(L), which gives the local average least-squares deviation of the integrated DOE of the unfolded eigenvalues from a straight line over an interval of length L, obtained for the wave numbers $\tilde{k}_l, \tilde{k}_u$ (circles), the eigenvalues of the quantum billiard (triangles), and Poissonian random numbers [red (gray) full line]. The agreement between the spectral properties of the Dirac billiard and the quantum

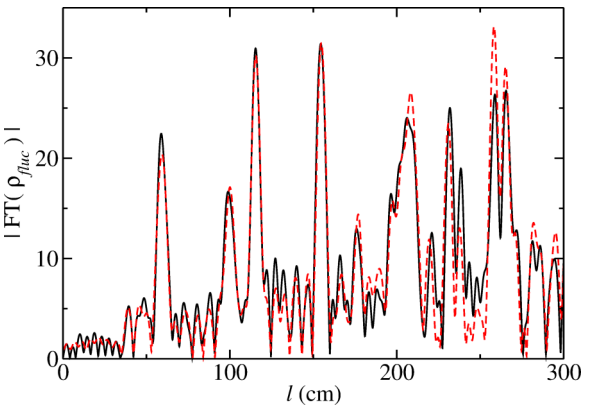

FIG. 13. (Color online) Comparison of the length spectrum of B1 in the lower Schrödinger region (full black line) with that of the corresponding quantum billiard (dashed red line).

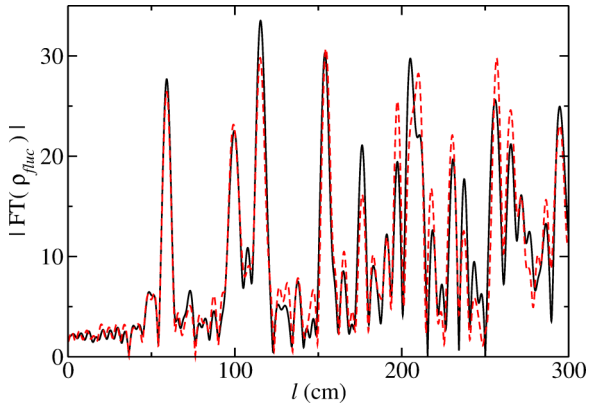

FIG. 14. (Color online) Same as Fig. 13 but for the upper Schrödinger region.

billiard is very good. This analogy, and also that of the TBM wave functions of the Dirac billiard and those of the rectangular quantum billiard, demonstrate that in the regions around the Γ points, that is, in the vicinity of the lower and upper band edges at k_{lBE} and k_{uBE}, the former is effectively described by the nonrelativistic Schrödinger equation of the latter.

We also determined the quasimomenta corresponding to the wave numbers $\tilde{k}_{S,n}$ of B1 and B2 directly using the TBM model. For this we computed the momentum distributions using the wave functions $\psi_n(x,y)$ obtained for each of them from the corresponding finite TBM:

$$\tilde{\psi}_n(\vec{k}) = \int_\Omega dx\,dy\,\psi_n(x,y)e^{-i(k_x x+k_y y)}\,. \tag{5}$$

They are peaked exactly at the momentum values $(k_x,k_y) = (q_x,q_y)$ associated with the eigenvalues $q_S = \sqrt{q_x^2+q_y^2}$ of the rectangular quantum billiard. Thus, the quasimomenta are indeed given by $\vec{q}_S = (q_x,q_y)$ in the Schrödinger region. This is in accordance with the conclusions drawn from the similarity between the wave numbers of B1 and the band-structure function $f(\delta\vec{q})$ shown in Fig. 9. These curves and thus the dispersion relation of the Dirac billiard are well described

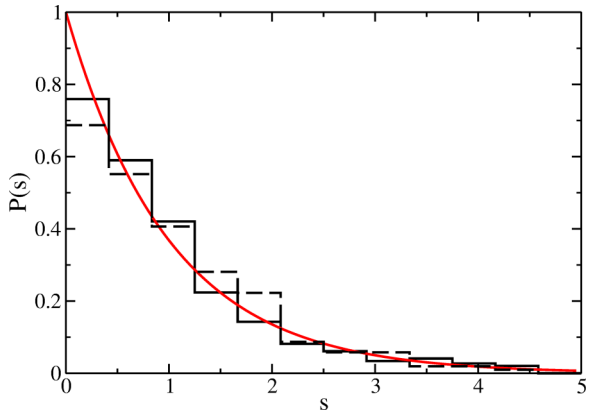

FIG. 15. (Color online) Comparison of the nearest-neighbor spacing distribution of B1 in the upper Schrödinger region (full black line) with that of the corresponding quantum billiard (dashed black line) and the Poisson distribution (full red line).

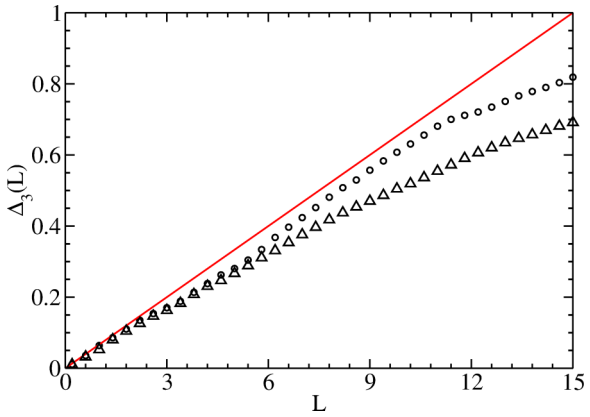

FIG. 16. (Color online) Comparison of the Δ_3 statistics of B1 in the upper Schrödinger region (circles) with that of the corresponding quantum billiard (triangles) and the Poisson distribution (full red line).

by a quadratic polynomial. Furthermore, we found that this analogy breaks down when the quasimomenta approach the border of the hexagonal BZ of the triangular lattice formed by the cylinders of the photonic crystal inside the Dirac billiard. Actually, the wave vectors of a rectangular quantum billiard are not restricted to it, and the wave-function patterns are the result of the superposition of the waves that are scattered at the cylinders, so we expect a deterioration of the analogy to occur whenever the triangular lattice structure prevails over the rectangular shape of the Dirac billiard. In the following section, we will consider the frequency region between the VHSs, where this indeed is the case.

B. Dirac region

The focus of this section are the spectral properties of billiard B1 in the vicinity of the Dirac frequency. For this we divided the wave numbers into spectra containing the first 100 ones above and below the Dirac wave number $k_D = 2\pi f_D/c$ with $\tilde{k}_{u,\tilde{n}} = k_n - k_D, n = 814,\ldots,913, \tilde{n} = n-813$ and $\tilde{k}_{l,\tilde{n}} = |k_n - k_D|, n = 714,\ldots,813, \tilde{n} = 814-n$, respectively, where $k_{n=813} < k_D < k_{n=814}$. Close to the Dirac frequency, the electromagnetic waves in billiards B1 and B2 are effectively described by the Dirac equation [28,49]. Accordingly, we compared their spectral properties with those of the corresponding rectangular graphene billiards with two opposite zigzag and two opposite armchair edges. Such billiards had been introduced in Ref. [21] to investigate spectral properties in graphene flakes. There, a transcendental equation for the corresponding eigenvalues q_{GB} was derived:

$$\kappa = \left(\mathrm{K} - \frac{m\pi}{L_{zz}}\right)\tan(\kappa L_{ac})\,,$$
$$q_{\mathrm{GB}} = \sqrt{\kappa^2 + \left(\mathrm{K} - \frac{m\pi}{L_{zz}}\right)^2}\,. \tag{6}$$

Here, $\mathrm{K} = \frac{4\pi}{3a_L}$ denotes the distance of the DPs, i.e., the corners of the first BZ from the Γ point at its center, and L_{ac} and L_{zz} are the lengths of the armchair and the zigzag edges, respectively. The eigenenergies of the graphene flake

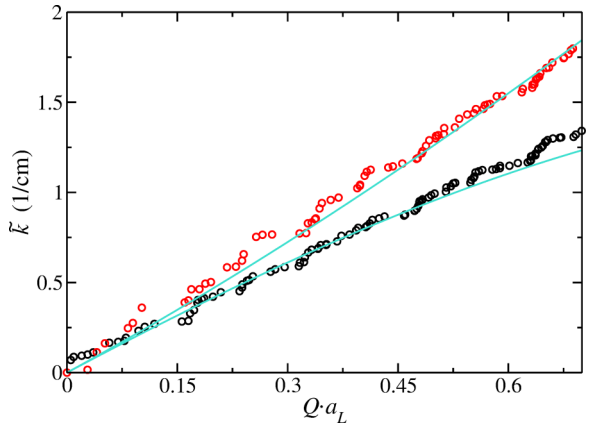

FIG. 17. (Color online) The first 100 wave numbers of B1 below ($\tilde{k} = \tilde{k}_l$, black) and above [$\tilde{k} = \tilde{k}_u$, red (gray)] the DP versus the eigenvalues $Q = q_D$ of the corresponding rectangular graphene billiard. The turquoise (light gray) curves show the band-structure function $\tilde{k} = 2\pi f(\delta\vec{q})/c$ versus the distance $Q = |\delta\vec{q}|$ from the DP. As may be guessed from the shape of the band structure shown in the right part of Fig. 4, deviations from a linear dispersion relation occur for smaller values of $|\delta\vec{q}|$ in the region below the DP than above.

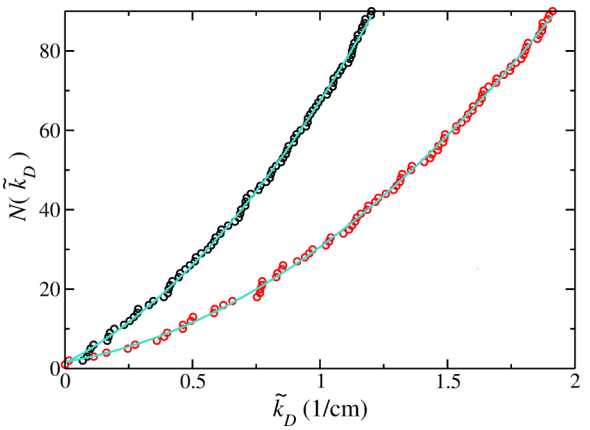

FIG. 18. (Color online) Integrated DOEs below ($\tilde{k}_D = \tilde{k}_l$, black) and above [$\tilde{k}_D = \tilde{k}_l$, red (gray)] the first DP of B1. Here, we skipped the ≈5 lowest eigenvalues. The quadratic polynomials best fitting the data [turquoise (light gray) full lines] are also depicted.

are obtained as $E = \hbar v_F q_{\rm GB}$, where v_F is graphene's Fermi velocity. On choosing the lengths L_{ac} and L_{zz} suitable for the modeling of the spectral properties of B1 and B2, one has to take into account that in graphene billiards the boundary conditions, i.e., the vanishing of the wave functions, are not imposed at the edges but for each of them at the first row of missing atoms. In Fig. 17, we plotted the wave numbers $\tilde{k} = \tilde{k}_l$ (black dots) and $\tilde{k} = \tilde{k}_u$ [red (gray) dots] versus the computed eigenvalues $Q = q_D = q_{\rm GB} - q_{\rm GB0}$ with $q_{\rm GB0}$ denoting the smallest eigenvalue. The turquoise (light gray) full lines show the band-structure functions $\tilde{k} = 2\pi f(\delta\vec{q})/c)$ in the regions below and above the DP versus the distance $Q = |\delta\vec{q}|$ of the quasimomentum vector $\vec{q}$ from the DP, respectively. They were computed as described in Sec. IV A. As in the Schrödinger region, the agreement between them and the experimental curves is good. Thus, as predicted in Ref. [21], in the vicinity of the DP the eigenvalues of the graphene billiard may be identified with the quasimomenta $|\delta\vec{q}|$. In order to corroborate this, we also determined the quasimomenta as outlined in Sec. IV A from the momentum distributions (5) associated with the wave functions computed from the finite TBM and found that, as expected, they are located at and close to the corners of the BZ.

As is visible in the figure, the wave numbers of B1 grow linearly with the eigenvalues of the rectangular graphene billiard, $\tilde{k}_D \propto q_D$, $\tilde{k}_D = \tilde{k}_l, \tilde{k}_u$. Consequently, as in the case of the latter, the dispersion relation is linear in the vicinity of the Dirac frequency

$$|f - f_D| = \frac{c}{2\pi}\tilde{k}_{l,u} = (v_D)_{l,u}\, q_D, \tag{7}$$

with v_D denoting the group velocity in B1. The difference in the slopes of the straight lines in Fig. 17 indicates that v_D takes different values below and above the Dirac wave number. The fits to the data points in the figure yielded $(v_D)_l \simeq 0.349c$ and $(v_D)_u \simeq 0.477c$. In fact, this inequality reflects the electron-hole asymmetry, i.e., the different opening angles of the lower and the upper cones observed in the band structure of graphene [58].

Furthermore, we compared the length spectra of B1 deduced from the wave numbers around k_D with those of the corresponding graphene billiard. For this we rescaled the experimental wave numbers $\tilde{k}_D = \tilde{k}_l, \tilde{k}_u$ so that their group velocities equaled that of the graphene billiard, which corresponds to multiplying the wave numbers with the inverse of the slopes of the straight lines in Fig. 17.

1. *Integrated DOE and length spectra*

The length spectra were obtained from the Fourier transform of the fluctuating part of the integrated DOE. In Fig. 18, we show the integrated DOE for the region below and above the DP, i.e., for $\tilde{k}_l$ as black circles and for $\tilde{k}_u$ as red (gray) ones, respectively. The turquoise (light gray) full lines show the quadratic polynomials

$$N_{\rm smooth}(\tilde{k}_{l,u}) \approx \frac{A}{2\pi}q_D^2 = \frac{A}{2\pi}\left(\frac{c}{(v_D)_{l,u}}\tilde{k}_{l,u}\right)^2 \tag{8}$$

that best fit the data. Here, A denotes the area of the Dirac billiard. We actually had to skip the ≈5 lowest eigenvalues around the DP, i.e., in the flat region around the DP in Fig. 8, in order to achieve that agreement. The difference between the integrated DOEs below and above k_D is due to that of the group velocities $(v_D)_l$ and $(v_D)_u$. As above, the fluctuating part $N^{\rm fluc}(\tilde{k}_D)$ of the integrated DOE was obtained by subtracting the smooth part Eq. (8) from it.

In Figs. 19 and 20, the length spectra computed from $N^{\rm fluc}(\tilde{k}_D)$ are compared with that deduced from the eigenvalues of the graphene billiard. The overall agreement is not as good as that found in the Schrödinger region between the experimental results and those for the corresponding quantum billiard (see Figs. 11 and 12). Deviations are especially observed in the amplitudes. Note that the boundary conditions differ a bit for the graphene billiard and the Dirac billiard. While for the former the wave functions vanish along the zigzag edges, this is not the case for B1, where they vanish along

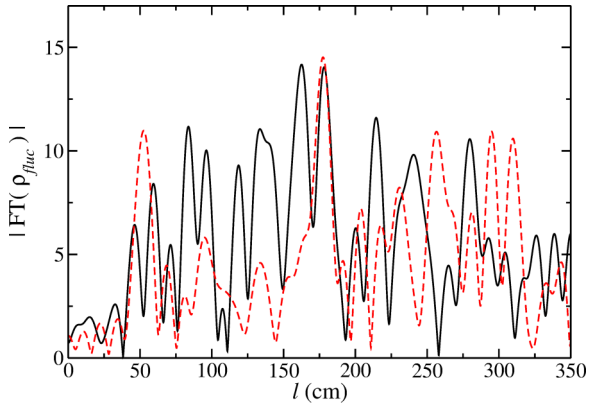

FIG. 19. (Color online) Comparison of the length spectrum of B1 in the region below the DP (full black line) with that of the corresponding graphene billiard (dashed red line). Altogether 90 wave numbers were taken into account.

the sidewalls of the cavity. These are slightly shifted with respect to the zigzag edges formed by the outermost rows of voids (see Figs. 1 and 2). Furthermore, deviations are expected because of the fluctuations of the experimental data around the straight line best fitting them (see Fig. 17), which reflects the correspondence between the wave numbers of B1 and the eigenvalues of the graphene billiard. Actually, they decrease with increasing q_D, i.e., wave number. Nevertheless, the number of eigenvalues is very low, so we are still far from the semiclassical regime. To check this, we compared the length spectrum of the graphene billiard obtained for the first 90 eigenvalues with that computed on the basis of the semiclassical trace formula for the DOE of the latter [21] in the corresponding energy range (see Fig. 21). Deviations similar to those in Figs. 19 and 20 are observed. Note, that the discrepancies decrease with increasing wave number and for large values of q_D the agreement has been shown to be excellent in Ref. [21]. We expect the same behavior for those visible in Figs. 19 and 20. Indeed, a comparison of the length spectrum for the graphene billiard with finite TBM calculations also revealed such deviations for spectra of comparable lengths. We thus conclude that a good agreement can only be achieved for very large graphene flakes.

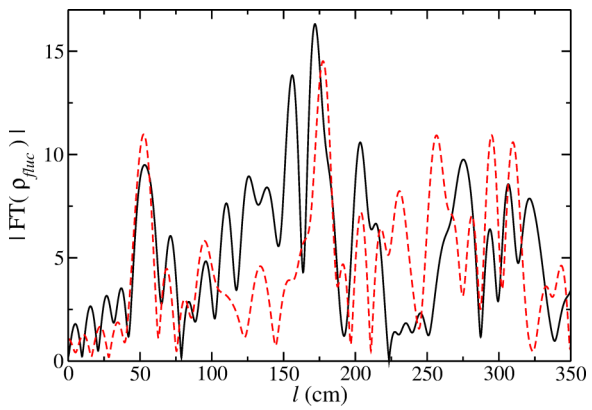

FIG. 20. (Color online) Same as Fig. 19 but in the region above the DP.

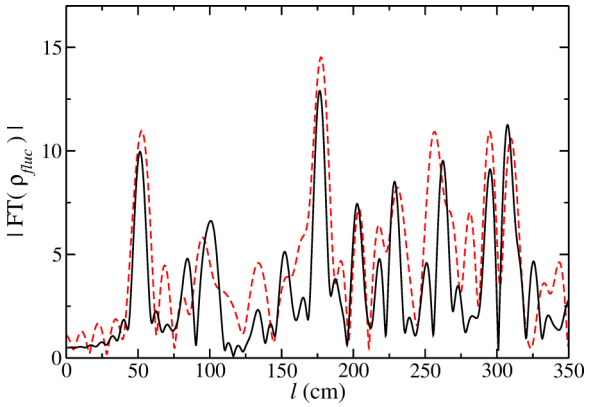

FIG. 21. (Color online) Comparison of the length spectrum of the graphene billiard (dashed red line) with that computed from the semiclassical trace formula for its DOE [21] (full black line). Altogether 90 eigenvalues were taken into account.

2. *Spectral properties of the wave numbers*

We also analyzed the spectral properties of the wave numbers $\tilde{k}_S = \tilde{k}_l, \tilde{k}_u$ by proceeding as described in Sec. IV A. Figure 22 shows as black full line the experimental result for the nearest-neighbor spacing distribution P(s), as black dashed line that for the eigenvalues of the rectangular quantum billiard, and as red (gray) full line the Poissonian distribution. Similarly, Fig. 23 shows the Dyson-Mehta statistic [18] Δ_3(L) obtained for the wave numbers $\tilde{k}_u$ (circles), the eigenvalues of the quantum billiard (triangles), and Poissonian random numbers [full red (gray) line]. The agreement between the spectral properties of the Dirac billiard and the graphene billiard is very good.

V. SECOND DIRAC POINT

In this section, we present results for the properties of the resonance spectrum of the Dirac billiard B1 shown in Fig. 3 in the two bands that frame the second DP. There, the band structure is more complicated than for the first DP, as can be guessed from the associated integrated DOE and the

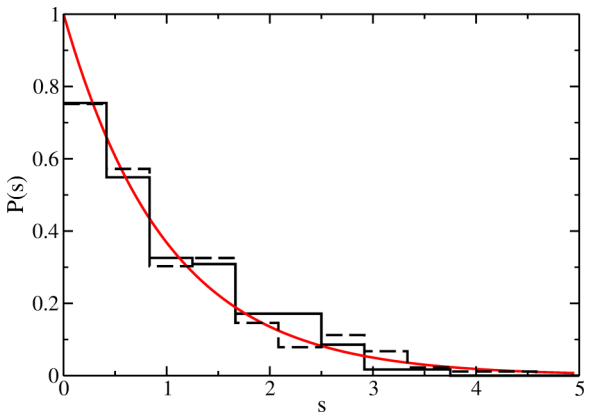

FIG. 22. (Color online) Comparison of the nearest-neighbor spacing distribution of the first 90 eigenfrequencies above the first DP of B1 (full black line) with that of the corresponding graphene billiard (dashed black line) and the Poisson distribution (full red line).

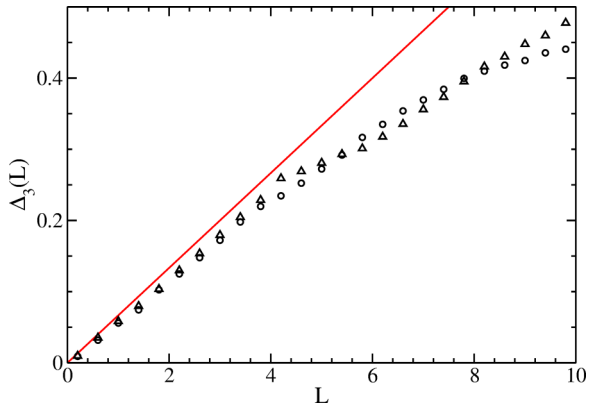

FIG. 23. (Color online) Comparison of the Δ_3 statistics of the first 90 eigenfrequencies above the first DP of B1 (circles) with that of the corresponding graphene billiard (triangles) and the Poisson distribution (full red line).

DOE shown as black curves in Figs. 24 and 25, respectively. The former exhibits a plateau around the Dirac frequency $f_D = 41.11$ GHz. Furthermore, it has two slight kinks at $f_{\rm VH}^- = 38.95$ GHz and $f_{\rm VH}^+ = 43.42$ GHz and, in distinction to the DOE for the two bands bracketing the first DP shown in Fig. 8, two more kinks at 44.49 GHz and at 46.63 GHz. They correspond to the sharp peaks observed above $f_{\rm VH}^+$ in the DOE shown in Fig. 25 and are marked by arrows in Fig. 24. The frequencies at the DP, f_D, the VHSs, $f_{\rm VH}^\pm$, and the lower and the upper band edges, $f_{\rm lBE}$ and $f_{\rm uBE}$, respectively, of the second DP are given in Table III. As can be deduced from Fig. 4, the peak at the highest frequency already is part of the subsequent band, which seems to start at the bottom of the sharp decline of the preceding one at $f_{\rm uBE} \approx 44.7$ GHz, whereas the lower band edge is at $f_{\rm lBE} = 33.66$.

The red (gray) curve in the upper panel of Fig. 25 shows the result of a fit of the TBM to the experimental DOE in the frequency range $f_{\rm lBE} \leqslant f \leqslant f_{\rm uBE}$. It reproduces the positions of the peaks, the band edges, and the DP of the latter,

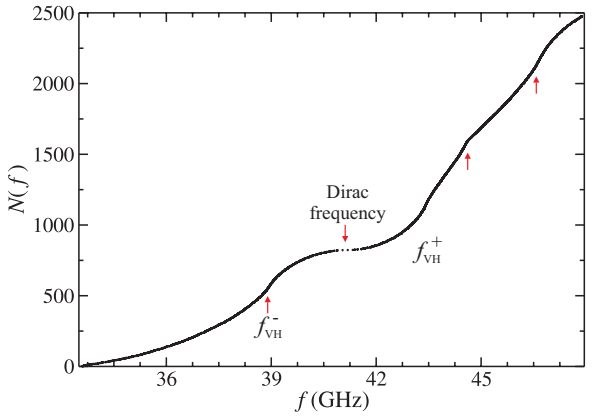

FIG. 24. (Color online) The integrated DOE $N(f)$ obtained from the resonance spectrum shown in Fig. 3 for the two bands joined at the second DP. It exhibits a plateau around the Dirac frequency $f_{\rm D} = 41.11$ GHz, where it barely varies, and slight kinks at the frequencies denoted by $f_{\rm VH}^- = 38.95$ GHz and $f_{\rm VH}^+ = 43.42$ GHz. At 44.49 and 46.63 GHz, two more kinks marked by arrows are clearly visible [32].

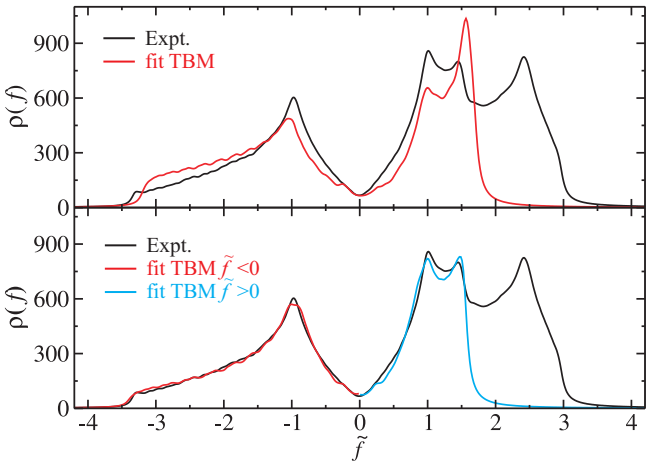

FIG. 25. (Color online) The DOE (black) obtained from the frequency spectrum shown in Fig. 3 for the same frequency range as the integrated DOE shown in Fig. 24. It is plotted versus the shifted and rescaled frequency $\tilde{f}$ which was obtained as described in the caption of Fig. 7. In the upper panel, it is compared to the DOE computed with the finite TBM [red (gray)]. The associated parameters were determined from a fit to the experimental DOE. In the lower panel, those obtained from fits in the frequency ranges below [red (gray)] and above [turquoise (light gray)] f_D are shown.

whereas the overall shape shows clear deviations. Note that the wavelengths, that vary from 9 to 6 mm in that frequency range, approach the value of the diameter of the cylinders and, consequently, the frequency dependence of the coupling parameters entering the TBM gets more and more crucial. Accordingly, in order to achieve a better agreement, we fit the finite TBM separately to the resonance density below and above the Dirac frequency. The resulting curves are shown in the lower panel in red (gray) and turquoise (light gray), respectively. The associated coupling and overlap parameters are given in Table IV.

The values of the overlap parameters are identical for the fits to the whole DOE (first row in Table IV) and to that above the DP (third row in Table IV) and, in distinction to those obtained arround the first DP (see Table II), are all of the same size. The coupling parameters except γ_3 are of comparable size. The parameters resulting from the fit to the DOE below (second row in Table IV) and above the DP, on the other hand, are of similar size except for the third coupling and overlap parameter, which is very small in comparison to s_2 for the former, as is the case for the first DP. Furthermore, the ratios γ_2/γ_1 and γ_3/γ_1 are by a factor of 5 larger than around the first DP. Consequently, the couplings and the wave-function overlaps between second- and third-nearest-neighboring sites of the lattice, respectively, are no longer negligible. This

TABLE III. Frequencies in GHz of the lower ($f_{\rm lBE}$) and the upper ($f_{\rm uBE}$) band edges, the second DP (f_D), and the VHSs ($f_{\rm VH}^\pm$) of billiards B1 and B2.

	$f_{\rm lBE}$	$f_{\rm VH}^-$	f_D	$f_{\rm VH}^+$	$f_{\rm uBE}$
B1	33.66	38.95	41.11	43.42	44.82
B2	34.87	39.21	41.38	43.61	45.13

TABLE IV. Coupling parameters in GHz and overlap parameters resulting from a fit of the DOE deduced from the finite TBM to the experimental one around the second DP. The first row gives the parameters obtained from the fit to the DOE in the whole frequency range $f_{\mathrm{lBE}} \leqslant f \leqslant f_{\mathrm{uBE}}$, the second and third one those for a fit to that below and above the DP at $f = f_D$, respectively.

	γ_0	γ_1	γ_2	γ_3	s_1	s_2	s_3
1.	−0.100	0.914	−0.053	−0.0017	0.044	0.039	0.0409
2.	0.229	−0.970	0.107	0.014	−0.051	−0.043	−0.0002
3.	−0.198	0.907	−0.093	0.110	0.044	0.039	0.0409

indicates that the applicability of the TBM and also the analogy of the wave equation governing billiards B1 and B2 to the Dirac equation expected in the vicinity of the DP, and found around the first and also the second one as outlined below, worsens with increasing frequency. Note that the signs of the parameters obtained from the fit to the DOE for frequencies $f \leqslant f_D$, i.e., when neglecting the double-peak structure above the DP differ from the corresponding ones resulting from the other two fits. A change of all signs corresponds to a reflection of the DOE at $f = f_D$. In fact, the DOE around the second DP seems to result from that around the first one by such an operation, as can be seen in Fig. 4.

Like for the first DP, we could divide the two bands around the second DP into regions, where the spectral properties coincide with those of a nonrelativistic quantum billiard and of a relativistic graphene billiard of corresponding shape, respectively. These are separated by the two VHSs.

A. Schrödinger region

Since the transition to the next band is not sharp, we only considered the first 250 wave numbers starting from the lower band edge $\tilde{k}_{l,n} = k_n - k_{\mathrm{lBE}}$, $n = 1, \ldots, 250$, for the comparison of the properties of the eigenfrequencies with those of the corresponding quantum billiard.

In Fig. 26, we plotted the wave numbers $\tilde{k} = \tilde{k}_l$ (black circles) versus the shifted eigenvalues $Q = q_S$ of the latter. The turquoise (light gray) curve shows the band-structure function $\tilde{k} = 2\pi f(\delta\vec{q})/c$, computed as described in Sec. IV A, as function of the distance $Q = |\delta\vec{q}|$ of the quasimomentum vector from the Γ point, i.e., the lower band edge. The good agreement between both curves demonstrates that, as in the case of the first DP, the quasimomenta may be identified with the eigenvalues of the quantum billiard. Both curves, and thus the dispersion relation in the frequency range below the first VHS, are well described by a quadratic polynomial. The wave functions obtained from the finite TBM have also the same structure as those of the latter. The intensity patterns, however, are not as clear-cut as for the first DP. Consequently, we observe larger deviations between the length spectra of B1 and the quantum billiard, shown in Fig. 27, than in Fig. 13. Still, the overall agreement, especially that of the peak positions, is good.

B. Dirac region

In order to investigate the spectral properties in the vicinity of the second DP, we divided the spectrum of wave

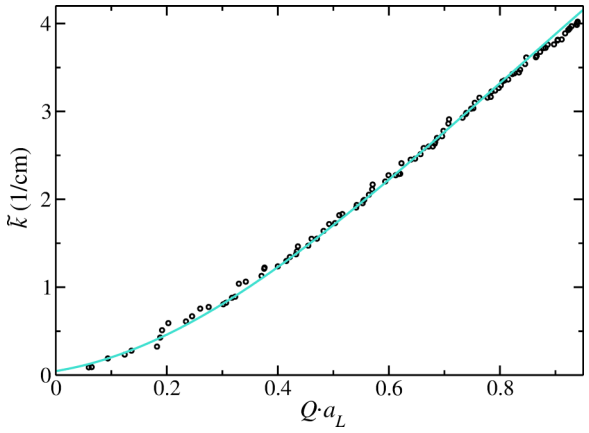

FIG. 26. (Color online) The first 250 wave numbers $[\tilde{k} = \tilde{k}_l)$ (black circles) with respect to the lower band edge $\tilde{k}_{\mathrm{lBE}}]$ versus the shifted eigenvalues $Q = q_S$ of the corresponding quantum billiard. The turquoise (light gray) shows the band-structure function $\tilde{k} = 2\pi f(\delta\vec{q})/c$ as function of the distance $Q = |\delta\vec{q}|$ of the quasimomentum vector from the lower band edge.

numbers into one for the first 100 above and below the Dirac wave number k_D, $\tilde{k}_{u,\tilde{n}} = k_n - k_D, n = 823, \ldots, 922, \tilde{n} = n - 822$ and $\tilde{k}_{l,\tilde{n}} = |k_n - k_D|, n = 723, \ldots, 822, \tilde{n} = 823 - n$, respectively, where $k_{n=822} < k_D < k_{n=823}$. Figure 28 shows the wave numbers $\tilde{k} = \tilde{k}_l$ (black circles) and $\tilde{k} = \tilde{k}_u$ [red (gray) circles] versus the eigenvalues of the corresponding rectangular graphene billiard $q_D = q_{\mathrm{GB}} - q_{\mathrm{GB0}}$ computed with Eq. (7), where q_{GB0} denotes the smallest eigenvalue. The turquoise (light gray) lines exhibit the band-structure function $\tilde{k} = 2\pi f(\delta\vec{q})/c$ as function of the distance $|\delta\vec{q}|$ of the quasimomentum vector $\vec{q}$ from the Dirac point. The good agreement demonstrates that also in the region around the upper DP, the quasimomenta may be identified with the eigenvalues of the graphene billiard. The curves are best fitted by a straight line. Thus, as in the vicinity of the first DP, the wave numbers of B1 grow linearly with the eigenvalues of the rectangular graphene billiard $\tilde{k}_D \propto q_D, \tilde{k}_D = \tilde{k}_l, \tilde{k}_u$. Consequently, the dispersion relation is also linear around the second DP. The difference in the slopes of the straight lines in Fig. 28, however, is much smaller than in Fig. 17. Accordingly,

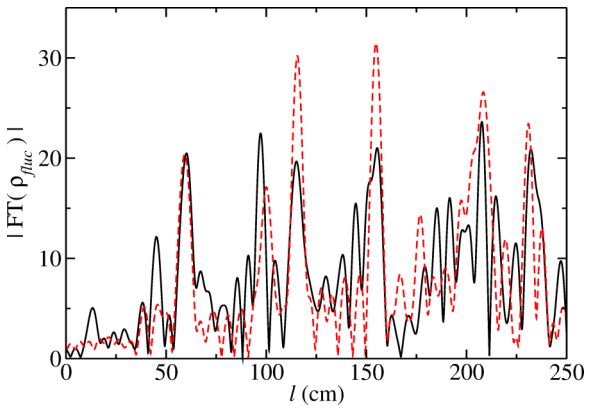

FIG. 27. (Color online) Comparison of the length spectrum of B1 in the lower Schrödinger region (full black line) with that of the corresponding quantum billiard (dashed red line).

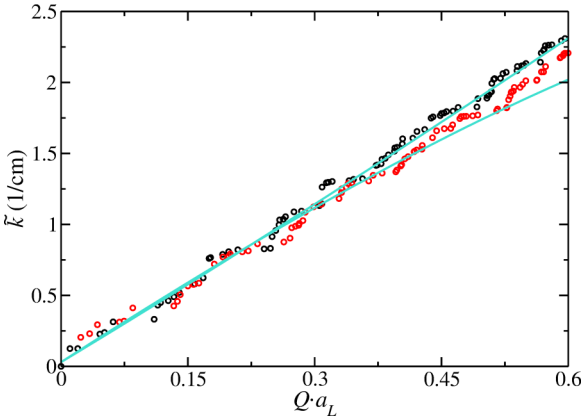

FIG. 28. (Color online) The first 100 wave numbers $\tilde{k} = \tilde{k}_l$ below (black circles) and $\tilde{k} = \tilde{k}_u$ above [red (gray) circles] the second DP versus those of the eigenvalues q_D of the corresponding rectangular graphene billiard. The turquoise (light gray) curves show the band-structure function $\tilde{k} = 2\pi f(\delta\vec{q})/c$ versus the distance $Q = |\delta\vec{q}|$.

the group velocities are approximately the same below and above the second DP, $(v_D)_l \simeq (v_D)_u$, where $(v_D)_l \simeq 0.608c$ and $(v_D)_u \simeq 0.561c$. Thus, the electron-hole asymmetry is not as pronounced as around the first one.

Furthermore, we compared the length spectra deduced from the wave numbers around k_D with those of the corresponding graphene billiard. For this, we again rescaled the experimental wave numbers $\tilde{k}_D = \tilde{k}_l, \tilde{k}_u$ so that their group velocities equal that of the graphene billiard. The agreement between the length spectra of B1 (black full line) and of the graphene billiard (red dashed line) below and above the DP in Figs. 29 and 30 is slightly better than for the first DP, shown in Figs. 19 and 20. The reason could be that the number of eigenvalues taken into account is larger (100 instead of 90). Like for the two bands framing the first DP, the spectral properties coincide with those of the quantum billiard and the graphene billiard and are well described by those of random Poissonian numbers in the regions below the lower VHS and between the VHSs, i.e., in the Schrödinger and the Dirac regions, respectively.

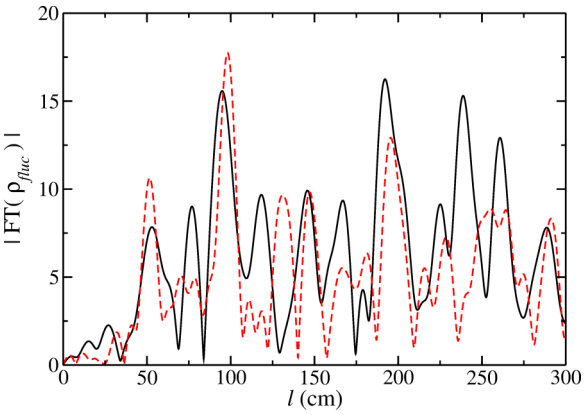

FIG. 29. (Color online) Comparison of the length spectrum of B1 in the region below the DP (full black line) with that of the corresponding graphene billiard (dashed red line). Altogether 100 eigenvalues were taken into account.

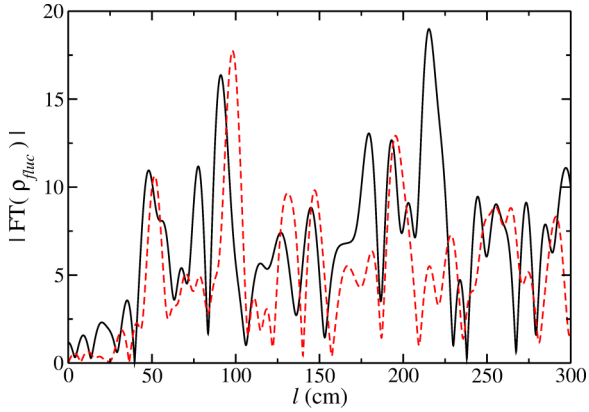

FIG. 30. (Color online) Same as Fig. 29 but in the region above the DP.

VI. CONCLUSIONS

We investigated the DOE and spectral properties like the nearest-neighbor spacing distribution and the Δ_3 statistics of two Dirac billiards in the two bands adjacent to the DP. For this purpose, we determined experimentally with unprecedented accuracy their eigenfrequencies by using superconducting microwave Dirac billiards. The resonance spectra comprised two DPs for both billiards. The associated DOE exhibits pairs of VHSs that bracket them. We demonstrated that the spectral properties and the length spectra are well reproduced by those of the graphene billiard of corresponding shape in the frequency region between them. Below and above that region, on the other hand, they are *identical* with those of the empty quantum billiard with the same shape. Accordingly, the wave equation governing the Dirac billiards is well approximated by the relativistic Dirac equation governing graphene billiards and the nonrelativistic Schrödinger equation describing quantum billiards, respectively. Note that generally works on properties of (artificial) graphene [13,14] only concentrate on the region around the DPs, whereas those beyond the VHSs are ignored, even though they exhibit these interesting features. In a previous publication [22], we associated the transition from the relativistic to the nonrelativistic region with a quantum phase transition similar to that occurring in the two-dimensional vibron model for transverse vibrations of molecules [59].

The results of this paper raise several questions. First, the considered Dirac billiards are rectangular and we found that their spectral properties coincide with those of random Poissonian numbers [17,56,57]. It would be of great interest to investigate those of a Dirac billiard with the shape of a classically chaotic one. Experiments with graphene quantum dots [8] found evidence that the spectral properties coincide with those of chaotic systems with violated time-reversal invariance, as predicted for chaotic neutrino billiards [15]. Numerical studies, however, revealed accordance with those of time-reversal-invariant systems, as is the case for non-relativistic Schrödinger billiards. These discrepancies were attributed to the boundary properties of graphene billiards, that may induce an intervalley scattering and thus a mixing of the two independent subsytems composing the honeycomb lattice. Experiments with a superconducting microwave Dirac

billiard, which has the shape of Africa [60], are in preparation. Another still open problem concerns the spectral properties of a Dirac or graphene billiard at the VHSs and also those in the flat band, where the DOE diverges logarithmically for an unbounded graphene sheet and exhibits sharp peaks for a finite one, as observable in Fig. 4. Due to their unprecedented accuracy, the experimental data dealt with in this paper are most suitable to tackle it and find an answer.

ACKNOWLEDGMENTS

This work was supported by the Deutsche Forschungsgemeinschaft (DFG) within the Collaborative Research Center 634. We are grateful to L. Hesse, F. Iachello, U. Kuhl, F. Mortessagne, K. Richter, H. Schomerus, and F. Wegner for stimulating discussions. Furthermore, we thank S. Bittner for his participation during the early stages of the work and C. Cuno, who performed preparatory experiments with both microwave Dirac billiards.

[1] K. S. Novoselov, A. K. Geim, S. V. Morozov, D. Jiang, Y. Zhang, S. V. Dubonos, I. V. Grigorieva, and A. A. Firsov, Science **306**, 666 (2004).
[2] A. H. Castro Neto, F. Guinea, N. M. R. Peres, K. S. Novoselov, and A. K. Geim, Rev. Mod. Phys. **81**, 109 (2009).
[3] A. Geim and K. Novoselov, Nat. Mater. **6**, 183 (2007).
[4] P. Avouris, Z. Chen, and V. Perebeinos, Nat. Nanotechnol. **2**, 605 (2007).
[5] C. W. J. Beenakker, Rev. Mod. Phys. **80**, 1337 (2008).
[6] D. Abergel, V. Apalkov, J. Berashevich, K. Ziegler, and T. Chakraborty, Adv. Phys. **59**, 261 (2010).
[7] F. Miao, S. Wijeratne, Y. Zhang, U. C. Coskun, W. Bao, and C. N. Lau, Science **317**, 1530 (2007).
[8] L. A. Ponomarenko, F. Schedin, M. I. Katsnelson, R. Yang, E. W. Hill, K. S. Novoselov, and A. K. Geim, Science **320**, 5874 (2008).
[9] R. M. Westervelt, Science **320**, 324 (2008).
[10] J. Güttinger, T. Frey, C. Stampfer, T. Ihn, and K. Ensslin, Phys. Rev. Lett. **105**, 116801 (2010).
[11] J. Güttinger, F. Molitor, C. Stampfer, S. Schnez, A. Jacobsen, S. Dröscher, T. Ihn, and K. Ensslin, Rep. Prog. Phys. **75**, 126502 (2012).
[12] F. Libisch, C. Stampfer, and J. Burgdörfer, Phys. Rev. B **79**, 115423 (2009).
[13] L. Huang, Y.-C. Lai, and C. Grebogi, Phys. Rev. E **81**, 055203 (2010).
[14] L. Huang, Y.-C. Lai, and C. Grebogi, Chaos **21**, 013102 (2011).
[15] M. V. Berry and R. J. Mondragon, Proc. R. Soc. London, Ser. A **412**, 53 (1987).
[16] X. Ni, L. Huang, Y.-C. Lai, and C. Grebogi, Phys. Rev. E **86**, 016702 (2012).
[17] O. Bohigas, M. J. Giannoni, and C. Schmit, Phys. Rev. Lett. **52**, 1 (1984).
[18] M. L. Mehta, *Random Matrices* (Academic, London, 1990).
[19] G. E. Mitchell, A. Richter, and H. A. Weidenmüller, Rev. Mod. Phys. **82**, 2845 (2010).
[20] J. Wurm, A. Rycerz, İ. Adagideli, M. Wimmer, K. Richter, and H. U. Baranger, Phys. Rev. Lett. **102**, 056806 (2009).
[21] J. Wurm, K. Richter, and İ. Adagideli, Phys. Rev. B **84**, 075468 (2011).
[22] B. Dietz, F. Iachello, M. Miski-Oglu, N. Pietralla, A. Richter, L. von Smekal, and J. Wambach, Phys. Rev. B **88**, 104101 (2013).
[23] A. Singha, M. Gibertini, B. Karmakar, S. Yuan, M. Polini, G. Vignale, M. I. Katsnelson, A. Pinczuk, L. N. Pfeiffer, K. W. West, and V. Pellegrini, Science **332**, 1176 (2011).
[24] L. Nádvorník, M. Orlita, N. A. Goncharuk, L. Smrčka, V. Novák, V. Jurka, K. Hruška, Z. Výborný, Z. R. Wasilewski, M. Potemski, and K. Výborný, New J. Phys. **14**, 053002 (2012).
[25] K. K. Gomes, W. Mar, W. Ko, F. Guinea, and H. C. Manoharan, Nature (London) **483**, 306 (2012).
[26] L. Tarruell, D. Greif, T. Uehlinger, G. Jotzu, and T. Esslinger, Nature (London) **483**, 302 (2012).
[27] T. Uehlinger, G. Jotzu, M. Messer, D. Greif, W. Hofstetter, U. Bissbort, and T. Esslinger, Phys. Rev. Lett. **111**, 185307 (2013).
[28] S. Bittner, B. Dietz, M. Miski-Oglu, P. Oria Iriarte, A. Richter, and F. Schäfer, Phys. Rev. B **82**, 014301 (2010).
[29] U. Kuhl, S. Barkhofen, T. Tudorovskiy, H.-J. Stöckmann, T. Hossain, L. de Forges de Parny, and F. Mortessagne, Phys. Rev. B **82**, 094308 (2010).
[30] E. Sadurni, T. H. Seligman, and F. Mortessagne, New J. Phys. **12**, 053014 (2010).
[31] S. Bittner, B. Dietz, M. Miski-Oglu, and A. Richter, Phys. Rev. B **85**, 064301 (2012).
[32] M. Bellec, U. Kuhl, G. Montambaux, and F. Mortessagne, Phys. Rev. Lett. **110**, 033902 (2013).
[33] M. Bellec, U. Kuhl, G. Montambaux, and F. Mortessagne, Phys. Rev. B **88**, 115437 (2013).
[34] M. C. Rechtsman, J. M. Zeuner, A. Tünnermann, S. Nolte, M. Segev, and A. Szameit, Nat. Photonics **7**, 153 (2013).
[35] M. C. Rechtsman, Y. Plotnik, J. M. Zeuner, D. Song, Z. Chen, A. Szameit, and M. Segev, Phys. Rev. Lett. **111**, 103901 (2013).
[36] A. B. Khanikaev, S. H. Mousavi, W.-K. Tse, M. Kargarian, A. H. MacDonald, and G. Shvets, Nat. Mater. **12**, 233 (2013).
[37] H.-J. Stöckmann and J. Stein, Phys. Rev. Lett. **64**, 2215 (1990).
[38] S. Sridhar, Phys. Rev. Lett. **67**, 785 (1991).
[39] H.-D. Gräf, H. L. Harney, H. Lengeler, C. H. Lewenkopf, C. Rangacharyulu, A. Richter, P. Schardt, and H. A. Weidenmüller, Phys. Rev. Lett. **69**, 1296 (1992).
[40] A. Richter, in *Emerging Applications of Number Theory*, The IMA Volumes in Mathematics and its Applications, edited by D. A. Hejhal, J. Friedmann, M. C. Gutzwiller, and A. M. Odlyzko (Springer, New York, 1999), Vol. 109, p. 479.
[41] M. Fujita, K. Wakabayashi, K. Nakada, and K. Kusakabe, J. Phys. Soc. Jpn. **65**, 1920 (1996).
[42] K. Nakada, M. Fujita, G. Dresselhaus, and M. S. Dresselhaus, Phys. Rev. B **54**, 17954 (1996).
[43] K. Sasaki, S. Murakami, and R. Saito, Appl. Phys. Lett. **88**, 113110 (2006).
[44] C. Dembowski, B. Dietz, T. Friedrich, H.-D. Gräf, H. L. Harney, A. Heine, M. Miski-Oglu, and A. Richter, Phys. Rev. E **71**, 046202 (2005).

[45] S. Joannopoulos, J. D. Johnson, R. Meade, and J. Winn, *Photonic Crystals. Molding the Flow of Light* (Princeton University Press, Princeton, NJ, 2008).
[46] L. Van Hove, Phys. Rev. **89**, 1189 (1953).
[47] H.-J. Stöckmann, *Quantum Chaos: An Introduction* (Cambridge University Press, Cambridge, 2000).
[48] H. Weyl, J. Reine Angew. Math. **141**, 1 (1912).
[49] S. Raghu and F. D. M. Haldane, Phys. Rev. A **78**, 033834 (2008).
[50] P. R. Wallace, Phys. Rev. **71**, 622 (1947).
[51] S. Reich, J. Maultzsch, C. Thomsen, and P. Ordejón, Phys. Rev. B **66**, 035412 (2002).
[52] F. Iachello and A. Del Sol Mesa, J. Math. Chem. **25**, 345 (1999).
[53] H. Schomerus, Opt. Lett. **38**, 1912 (2013).
[54] M. C. Gutzwiller, J. Math. Phys. **11**, 1791 (1970).
[55] M. C. Gutzwiller, J. Math. Phys. **12**, 343 (1971).
[56] G. Casati, F. Valz-Gris, and I. Guarnieri, Lett. Nuovo Cimento **28**, 279 (1980).
[57] M. V. Berry, Eur. J. Phys. **2**, 91 (1981).
[58] B. Huard, N. Stander, J. A. Sulpizio, and D. Goldhaber-Gordon, Phys. Rev. B **78**, 121402 (2008).
[59] F. Iachello and S. Oss, J. Chem. Phys. **104**, 6956 (1996).
[60] M. V. Berry and M. Robnik, J. Phys. A: Math. Gen. **19**, 649 (1986).